Integration of Silica Nano-rattles with Manganese-doped In_2S_3/InOOH to Enable Ultrasound-mediated Tumor Theranostics

Tian Zhang[1, ‡], Qiang Zheng[2, ‡], Congkun Xie[1], Gonglin Fan[2], Yifan Wang[2], Yongjun Wu[1], Yike Fu[1,3], Jie Huang[4], Duncan Q.M. Craig[5], Xiujun Cai[2]*, Xiang Li[1,3]**

[1] State Key Laboratory of Silicon Materials, School of Materials Science and Engineering, Zhejiang University, Hangzhou, Zhejiang 310027, P. R. China

[2] Key Laboratory of Endoscopic Technique Research of Zhejiang Province, Sir Run Run Shaw Hospital, Zhejiang University, Hangzhou 215123, P. R. China

[3] ZJU-Hangzhou Global Scientific and Technological Innovation Center, Zhejiang University, Hangzhou, 311200, P.R. China.

[4] Department of Mechanical Engineering, University College London, London WC1E 7JE, UK

[5] University College London School of Pharmacy, London WC1N 1AX, UK

* Corresponding Author: fyk3927@zju.edu.cn; srrsh_cxj@zju.edu.cn; xiang.li@zju.edu.cn (XL)

‡ Authors with equal contribution

KEYWORDS. Sonodynamic therapy, ultrasound imaging, heterostructure, Indium, rattle-type SiO_2.

ABSTRACT. As a result of their radiation-free nature and deep-penetration ability, tumour theranostics mediated by ultrasound have become increasingly recognized as a modality with high potential for translation into clinical cancer treatment. The effective integration of ultrasound imaging and sonodynamic therapy (SDT) into one nanoplatform remains an enormous challenge yet to be fully resolved. Here, a novel theranostic system, consisting of rattle-type SiO_2 (r-SiO_2) loaded with Mn doped In_2S_3/InOOH (SMISO), was designed and synthesized to enable an improved ultrasound imaging-guided therapy. With Mn doping In_2S_3/InOOH (MISO) and heterojunction structure, this novel sonosensitizer facilitates the generation of reactive oxygen species (ROS) for SDT. By coupling interfaces between shell and core in rattle-type SiO_2, multiple reflection/scattering are generated, while MISO has high acoustic impedance. Integrating r-SiO_2 and MISO, the SMISO composite nanoparticles (NPs) increase acoustic reflection and provide enhanced contrast for ultrasound imaging. Through the effective accumulation in tumors, which was monitored by B-mode ultrasound imaging *in vivo*, SMISO composite NPs effectively inhibited tumor growth without adverse side effects under ultrasound irradiation treatment. This work therefore provides a new approach to integrate novel gas-free ultrasound contrast agent and semiconductor sonosensitizer for cancer theranostics.

1. Introduction

Cancer is a leading cause of death worldwide, accounting for nearly 10 million fatalities in 2020 [1]. Nanomedicine and diagnostic agent has been applied to reduce cancer mortality, while the efficacy of tumor therapy is seriously limited by the complexity and heterogeneity of tumors. In order to improve the treatment efficacy and reduce the toxic side effects, numerous researchers have focused attention on noninvasive external field-mediated theranostic systems, which integrate tumor diagnosis and treatment into one nanoplatform.[2, 3] Ultrasound is a popular nondestructive and deep-penetration diagnostic tool that is widely accepted and employed in clinics. The combination of ultrasound-based diagnosis and therapy is expected to realize effective therapeutic functions without adverse side effects.[4, 5]

Ultrasound imaging, implemented by the pulse-echo principle of ultrasound, has the advantages of radiation-free nature, clinical practicality, and real-time operation.[6, 7] The introduction of contrast agents could ameliorate the inherent limited spatial resolution of ultrasound. Gas-filled microbubbles, which utilize the total reflection of ultrasound onto the liquid-gas interface, can act as contrast agents to improve the resolution and sensitivity of enhanced ultrasound imaging.[7-9] Indeed, microbubble contrast agents and their targeted imaging approaches have been applied to the field of molecular imaging and targeted therapy.[10, 11] Nevertheless, the current bubble contrast agents are usually in micro-scale (1-10 μm) and hence may not traverse the endothelial gap of blood vessel after intravenous injection, hence they may become trapped in the blood pool, and act effectively only as angiographic agents.[12] To extend the application of ultrasound contrast agents in probing deep tissues, a series of nanoscale bubbles and nanodroplets have been studied, including nano-liposome contrast agent with reflective properties and nano-fluorocarbon emulsions (perfluoropentane (PFP), or perfluorohexane (PFH)) with liquid-gas phase transition

properties.[13-16] However, these systems still use gas as the basis of reflection, thus suffering from the problems of poor stability and short duration of intravital imaging. Therefore, gas-free systems with a liquid-solid interface to realize high-intensity reflection and scattering of ultrasound onto the surface may provide a new approach to achieve a prolonged, stable and efficient tissue imaging. Considering that the reflection intensity is principally affected by the density and acoustic impedance of materials, loading nanoparticles with high acoustic impedance onto the surface of the contrast agent can be an effective method to further enhance the reflective abilities and the contrast of tissue sonography.[17, 18]

In addition, sonodynamic therapy (SDT) is an emerging treatment for cancer, which utilizes low-intensity ultrasound to activate sonosensitizers to induce intracellular oxidative stress, generate reactive oxygen species (ROS) and hence kill the tumor cells.[19, 20]. Sonosensitizers play a vital role in the process of SDT, and increasing efforts have been exploring the advantages of inorganic nanoparticles, such as semiconductors, as a new type of sonosensitizer.[21-23] Activated electrons and holes generated in semiconductors could participate in the redox reaction to produce ROS when promoted by the absorption of ultrasound.[24, 25] However, the fast recombination of electrons and holes can limit the ultrasonic catalytic activity of semiconductors. Heterojunction structures and metal ion doping have been effective approaches to facilitate electron-hole separation and improve the quantum yield.[26-28] Various nano-platforms which integrated ultrasonic diagnosis and treatment have been developed, but those systems are still gas-based, examples including stable gas-generating nanoparticles ($CaCO_3$, double-layer hollow manganese silicate nanoparticles (DHMS), etc.) at the tumor sites and in situ stimuli-responsive (pH, H_2O_2 etc.) nanobubbles.[29, 30]. Therefore, combining SDT-based therapeutic agents with contrast agents characterized by liquid-

solid interfaces is a potentially highly promising approach but one whereby current understanding and development has been lacking.

Here, we designed a composite system involving the assembly of Mn doped In_2S_3/InOOH (MISO) onto rattle-type SiO_2. This SMISO nano-platform can simultaneously serve as a sonosensitizer and a contrast agent. MISO was obtained *via* a one-step hydrothermal method and rattle-type SiO_2 (r-SiO_2) was synthesized by etching solid-SiO_2/hollow-SiO_2 (s/h SiO_2) (**Scheme 1**). In this system, r-SiO_2 with two layers of contributing interfaces which could provide multiple reflection/scattering for ultrasound imaging. MISO with high acoustic impedance could further strengthen ultrasonic signals and enhance the contrast of ultrasound imaging. Besides, the innovative design of MISO composite could improve the electron-hole separation efficiency by tuning the band gap structure, thus promoting the SDT performance. This study examines both the therapeutic efficacy and imaging capability SMISO NPs *in vitro* and *in vivo,* thereby exploring this novel strategy as a potentially highly useful means of achieving deep tissue theranostic activity.

2. Materials and Methods

2.1. Chemicals and agents. All the regents were analytical purity or better and used without further treatment. Ammonia solution (NH_3 H_2O), tetraethyl orthosilicate (TEOS), sodium carbonate anhydrous (Na_2CO_3), manganese (II) chloride tetrahydrate ($MnCl_2$ $4H_2O$), nitric acid (HNO_3, 69 wt.%) and hydrochloric acid (HCl) were purchased from Sinopharm Chemical Reagent Co., Ltd. 3-aminopropyltriethoxysilane (APTES), Sodium sulfide nonahydrate ($Na_2S{\cdot}9H_2O$) and Indium (III) nitrate hydrate ($In(NO_3)_3$) were purchased from Macklin. 1, 3-Diphenylisobenzofuran (DPBF) were obtained from Aladdin Co., Ltd. Polyethyleneimine (PEI) and 2',7'-Dichlorodihydrofluorescein diacetate (DCFH-DA, ≥97%) were obtained from Sigma-Aldrich.

2.2. Characterization. The micro-morphology and microstructure of materials were observed using field-emission scanning electron microscopy (FESEM, Phenom LE) and transmission electron microscopy (TEM, 200 kV/JEOL JEM-2010HR). The energy-dispersive X-ray spectroscopy (EDS) were characterized to measure the chemical compositions. The X-ray diffraction analysis were performed on a Rigaku D/Max-2550pc powder diffractometer, scanning 2θ from 5° to 80°. The X-ray photoelectron spectroscopy (XPS) was used on AXIS Supra, Kratos to characterize the valence state of the composites. The UV-Vis absorption spectroscopy and the solid diffuse reflectance spectra (DRS) were recorded on a UV-2600 UV-Vis spectrophotometer (Shimadzu). The ESR spectra were measured by Bruker A300 X-band EPR spectrometer.

2.3. Synthesis and surface modification of rattle-type SiO_2.[17] Firstly, 35.7 mL of ethanol, 5 mL of ultra-pure water and 1.57 mL of ammonia solution were mixed and stirred at 30℃ for 30 min. Then 3 mL of tetraethyl orthosilicate (TEOS) was injected into the above solution and the stirring was continued for another 45 min. Then the mixture of 2.5 mL of TEOS and 1 mL of 3-aminopropyltriethoxysilane (APTES) was added quickly and reacted for another 75 min. After that, the as-prepared s/h SiO_2 NPs were centrifuged and washed with water and ethanol for three times and resuspended in 40 mL of water.

4 mL of as-prepared s/h SiO_2 suspension was mixed with 6 mL Na_2CO_3 solution (1 M) and stirred at 80℃ for 30 min, 1 h and 3 h, forming the targeted product rattle-type SiO_2. Then the suspension was centrifuged and washed with water for three times and redispersed in 4 mL of water. To modify the r-SiO_2 NPs, 4 mL of r-SiO_2 solution and 100 μL of PEI solution (20 mg/mL) were mixed and stirred at room temperature for 3 h. Then the mixture was centrifuged, washed with water for three times and resuspended in 4 mL of water for further use.

2.4. Synthesis of Mn doped In_2S_3/InOOH nanoparticles (MISO). Mn doped In_2S_3/InOOH nanoparticles were synthesized using a hydrothermal method.[31] Briefly, 72 mg of $In(NO_3)_3$ and 3.5 mg of $MnCl_2 \cdot 4H_2O$ were solubilized with 10 mL of water and then the solution was added dropwise into 10 mL of Na_2S solution (0.06 M). After that, the pH of the mixture was adjusted to 2.67 and the mixture was subsequently stirred for another 10 min. Afterwards, the solution was transferred to a 50 mL Teflon-lined stainless steel autoclave and maintained at 180 ℃ for 12 h. After cooling down to room temperature, the suspension was centrifuged, washed with water for three times and resuspended in 20 mL of water for further use.

2.5. Synthesis and surface modification of r-SiO_2@Mn-In_2S_3/InOOH composites (SMISO). In a typical process, 4 mL of r-SiO_2-PEI solution was mixed with 12 mL of Mn-In_2S_3/InOOH and stirred overnight to form the r-SiO_2@Mn-In_2S_3/InOOH composites. The suspension was centrifuged, washed with water for three times and resuspended in 12 mL of water. Then 2 mL of the r-SiO_2@Mn-In_2S_3/InOOH solution was mixed with 20 mL of BSA solution (0.5 mg/mL) and stirred for 3 h to modify the surface of composite.

2.6. ROS generation of MISO and SMISO composites. The detection of ROS generated by MISO and SMISO composites upon ultrasound irradiation was performed by using 1, 3-Diphenylisobenzofuran (DPBF) as a ROS indicator. Briefly, 100 μL of DPBF (2 mM) was injected into 3 mL of 60 μg/mL sample solution (MISO with different Mn doping concentrations). Subsequently, the mixture was irradiated with ultrasound (1.0 MHz, 1.0 W/cm^2) in the dark and the UV-Vis absorption of the reaction solution was measured every 2 minutes. Besides, the optical density of DPBF solution at 415 nm was used as an index of ROS production to assess the ROS production ability of different samples. The DPBF degradation ability of sample solution without ultrasound treatment was also examined following the similar protocol.

To study the SDT effect of SMISO under neutral and acidic conditions, SMISO NPs were mixed with PBS at different pH values (7.4 and 5.5) and reacted at 37 ℃ for 2 h. And the supernatant was harvested after a low-speed centrifugation. Then ROS generation activity of the supernatant under ultrasound irradiation was measured in the same way as described above.

2.7. ESR measurement. TEMP and DMPO probe were used to detect the generated $^1O_2$ and ·OH, respectively. Briefly, after US irradiation for 2 min, 160 μl 1-MISO solution (60 μg/mL) was added to TEMP (40 μl) or DMPO (40 μl), and the resultant TEMP-$^1O_2$ and DMPO-OH adduct was detectable by ESR spectrometer.

2.8. Reflection and scattering measurement. For the reflection and scattering measurements, a waveform generator (Keysight 335008) and the transducer centering at 1.5 MHz were used for the whole test. The samples were placed at 18 cm meter away from the main transducer and the sample stage was aligned with the transducer. The transducer emitted ultrasound wave and subsequently receive the reflected ultrasound wave in the reflection measurement. In the scattering measurement, another transducer laying at an angel of 90° and tightly adhering to the sample stage was employed and served as the receiving transducer.

2.9. Cell culture. 4T1 murine breast cancer cells, kindly provided by Sir Run Shaw Hospital, Zhejiang University, were utilized for the *in vitro* and *in vivo* studies. 4T1 cells were cultured in RPMI 1640 medium with 10% fetal bovine serum (FBS) and incubated at 37 ℃ in a humidified incubator of 5% CO_2.

2.10. SDT performance *in vitro*. The SDT performance *in vitro* of SMISO was investigated by measuring the cell viabilities after different treatments *via* MTT assay. In brief, the cells were seeded in 35 mm culture dishes at a density of 10^6 cells/dish and cultivated for 12-16 h. After that,

the medium was replaced with serum-free medium containing SMISO with different concentrations (0-200 μg/mL). After incubated for 2 h, the dishes were treated with or without US irradiation (1.0 MHz, 1.0 W/cm^2, 3 min) and supplemented with 150 μL of FBS per dish. Then the cells were cultured for another 24 h and the medium was replaced with 10 % MTT solution and incubated at 37℃ for another 2 h. Finally, the MTT solution was replaced by DMSO to dissolve the crystals. The absorbance at the wavelength of 560 nm was measured using a microplate reader. As a comparison, the SDT effect of SiO_2 (100 μg/mL) and MISO (50 μg/mL) was also detected in the same way.

2.11. Live&dead assay and cell apoptosis analysis. To prove the killing effect to the cells, the live and dead cells were stained with calcein-AM/ propidium iodide (PI) according to the above conditions. After US treatment for another 6 h, the cells were cultured with fresh medium containing calcein-AM (4 μmol/L) and PI (8 μmol/L) at 37℃ for 30 min, and then observed by fluorescent microscope (Nexcope NIB900) under blue and green light excitation. In addition, the cell apoptosis analysis was also conducted by flow cytometry according to the similar treatment as live&dead assay. The cells were co-stained with Annexin V–fluorescein isothiocyanate (FITC) (5 μL) and PI (5 μL) for 15 and 5 min, respectively and monitored by flow cytometry.

2.12. ROS detection *in vitro*. The intracellular ROS was monitored by fluorescence probe 2′,7′-dichlorofluorescein diacetate (DCFH-DA), which could be transformed into green fluorescence DCF based on ROS-dependent oxidation in the cell. Briefly, after seeded for 12-16 h, the cells were incubated with different materials (SiO_2, MISO, SMISO) for another 2 h. Then, the cells were treated with or without US irradiation (1.0 MHz, 1.0 W/cm^2, 3 min), stained with DCFH-DA probe. At last, the cells were monitored by fluorescence microscope qualitatively and flow cytometry quantitatively.

2.13. Animal model. All animal experiments were supported by the Ethics Committee of Sir Run Run Shaw Hospital (ZJU20220345) and 4-6 weeks old female Balb/c nude mice were purchased from Shanghai Laboratory Animal Center. The animal model used in our experiments was constructed as previously reported. 4T1 cell tumor model was established by subcutaneous injecting 50 μL of PBS containing 2×10^6 cells into the left side abdomen of nude mice.

2.14. Ultrasound imaging *in vitro* and *in vivo*. Ultrasound imaging was carried out using a preclinical ultrasound imaging platform GE LOGIQ 9 unit (GE Healthcare, Waukesha, USA) and the linear probe (9 L) was used to receive the acoustic signals. For the *in vivo* US imaging, the tumor-bearing mice were anesthetized and intravenously injected with SMISO (15 mg/kg) via the tail vein and the signals were monitored at different time points. As a supplement, SiO_2 (10 mg/kg), MISO (5 mg/kg) and SMISO (15 mg/kg) were intratumorally injected and ultrasound imaging of mice was conducted at 5 min post-injection.

2.15. *In vivo* SDT study. The tumor treatment was initiated when tumor reached a volume of ~100 cm^3. The tumor-bearing mice were randomly assigned into 6 groups of 5 mice per group and received the intravenous injection of different materials and treated with or without ultrasound irradiation as described below: (1) Control (normal saline), (2) US alone (1.0 MHz, 1.5 W/cm^2, 2 min), (3) SiO_2 + US (10 mg/kg, i.v. injection), (4) MISO + US (5 mg/kg, i.v. injection), (5) SMISO alone (15 mg/kg, i.v. injection), (6) SMISO + US (15 mg/kg, i.v. injection). At 12 h and 24 h after administration, the relative mice were anesthetized for ultrasound irradiation. The administration protocol was repeated three times every five days in 15 days. Furthermore, the body weight and tumor volume of each mouse were measured every two days in 15 days. The tumor volume was calculated in accordance with the following formula: $width^2 \times length/2$. The mice were sacrificed at the end of the treatment, after which the subcutaneous tumors were peeled off, imaged and

weighed. After fixed with 4 % paraformaldehyde solution for 48 h, the tumor tissues were dehydrated, embedded in paraffin and sectioned. Then the slices were stained with hematoxylin-eosin (H&E) and Ki67 and observed by optical microscopy for histopathological analysis. In addition, at 12 h after administration, the mice groups with different treatments were anesthetized for ultrasound irradiation, and subsequently the tumor slices were collected, frozen, fixed and stained using dihydroethidium (DHE) and DAPI successively for 30 min at 37℃ for ROS staining. The fluorescence images were monitored by a fluorescence microscope (NIKON ECLIPSE E100).

2.16. Biosafety evaluation. The biosafety of SMISO was assessed by histopathological analysis, biodistribution experiment, blood biochemistry and blood routine examination. Briefly, the major organs were harvested at 5 h, 12 h, 24 h and 72 h post injection of SMISO. Then the tissue samples were weighed and digested with 10 mL of nitric acid/perchloric acid (9:1) at 255 ℃ and the concentration of In was determined by ICP-OES. Also, the blood was collected from the eyeball of mice at pre-injection, 1-day post-injection, 3-days post-injection and 7-days post-injection of SMISO for blood routine test and blood biochemical test.

3. Results and discussion

3.1. Synthesis and functional characteristics of SMISO NPs

SMISO nanoparticles (NPs) were synthesized by loading the as-prepared Mn doped In_2S_3/InOOH (MISO) NPs onto the surface of etched rattle-type SiO_2 (r-SiO_2) (Scheme 1). HNO_3, $MnCl_2$ and $In(NO_3)_3$ were dispersed in Na_2S solution and then MISO with Mn/In feeding molar ratios of 0%, 1% and 5% were obtained by a one-step hydrothermal method.[31] From the transmission electron microscopy (TEM) images (**Figure 1**a and **Figure S1**, Supporting Information), the MISO NPs with two different Mn doping concentrations show irregular

polyhedral morphology with similar particle sizes (15±5 nm) and distinct lattice fringes were observed in 1-MISO, which are corresponding to the (110) plane of InOOH and the (107) plane of β-In_2S_3. The XRD patterns of MISO with two Mn doping concentrations are also similar (Figure 1b). MISO NPs are crystallized and the main peaks are matched well with those of β-In_2S_3 phase (JCPDS 25-0390) and InOOH phase ((JCPDS 17-0549). To verify the successful doping of Mn, the contents of Mn and In were examined by ICP-OES, confirming the doping content of Mn element in the samples of 0-MISO, 1-MISO and 5-MISO (Figure S2). Subsequently, in order to investigate the SDT property of MISO NPs, the reactive oxide specie probe 1,3-diphenylisobenzofuran (DPBF) was employed to study the ability of sono-induced ROS generation by MISO. As shown in Figure S3, without US irradiation, the degradation of DPBF was of low magnitude in the presence of MISO with different Mn doping concentration due to the adsorption by MISO. In contrast, as demonstrated in Figure 1c and **Figure S4**, the characteristic absorption of DPBF at 415 nm showed a marked decrease as US irradiation time proceeds. The results show that In_2S_3/InOOH itself (0-MISO) possesses a SDT performance and1-MISO has the strongest SDT performance. When exposed to US for 8 min, the degradation of DPBF in 0-MISO, 1-MISO and 5-MISO solutions are 46%, 99.5% and 85%, respectively. With increasing the amounts of Mn doping, the performance decreased, 1-MISO had an optimum SDT efficiency and DPBF in this group was completely degraded after US irradiation for 10 min. With further increase of Mn doping concentrations, the SDT performance was not higher. To clarify the type of ROS generated, ESR spectra were conducted using TEMP and DMPO probe (Figure S5), and the appearance of ESR signals showing three characteristic peaks with a ratio of 1:1:1 for TEMP-$^1O_2$ indicated the production of $^1O_2$ during the SDT process of 1-MISO. In addition, MISO with different Mn doping concentrations show negligible ROS production (Figure S6).

To understand the mechanism of this phenomenon, the optical absorption, band variation and charge transfer capacity of MISO with different Mn doping concentrations were measured. As shown in UV-visible diffuse reflectance spectra (**Figure S7** and Figure 1d), 1-MISO exhibits higher light absorption compared with 0-MISO and 5-MISO, indicating its higher ultrasound absorption during SDT process. The broad and strong absorption bands of MISO indicate an internal bandgap transition from the valence band (VB) to the conduction band (CB). A Tauc plot was used to calculate the bandgap of MISO according to the Kubelka–Munk formula; the bandgaps of 0-MISO, 1-MISO, 5-MISO were 3.72 eV, 2.68 eV and 3.24 eV, respectively. The bandgap of 1-MISO is narrower than that of 0-MISO and 5-MISO, which implies greater production of activated electrons (e^-) and holes (h^+) during the SDT process. According to the electrochemical impedance spectrum (EIS) Nyquist plots of MISOs (Figure 1e), 1-MISO has the smallest semicircle between 0-MISO and 5-MISO, indicating the reduced charge transfers resistance and promotes charge separation efficiency. Therefore, 1-MISO was chosen as the optimum sonosensitizer in this study. A putative mechanism is proposed in Figure 1f. The bandgaps of InOOH and In_2S_3 are 3.75 eV and 2.12 eV, respectively, hence these two semiconductors could absorb the ultrasound energy to induce the separation of e^- and h^+.[32] More specifically, under US irradiation, the electronic transition between InOOH and In_2S_3 could induce the activated electrons to transfer from the CB of In_2S_3 to that of InOOH and the activated holes to transfer from the VB of InOOH to that of In_2S_3, according to the principle of the lowest energy and the difference of Fermi level. In addition, the metal ion doping induces the formation of defect energy level near the CB of In_2S_3 and InOOH, thus capturing the electrons and disrupting electron-hole recombination.[33] The concentration of Mn can also change the content of In_2S_3 and InOOH in MISO. The redundant defects could be introduced by the excessive Mn which might result in the

recombination of e^- and h^+ instead. It could be concluded that the synergism between heterojunction and ion doping effectively separate e^- and h^+ and promote the quantum yield, thereby significantly enhancing the sono-induced ROS generation.

r-SiO_2 NPs were synthesized via etching solid-SiO_2/hollow-SiO_2 (s/h SiO_2) NPs at 80 ℃ for one hour.[17] From the scanning electron microscopy (SEM) and TEM micrographs (**Figure S8**), the s/h SiO_2 NPs maintain good dispersity and have a relatively uniform spherical morphology with an average diameter of 205±25 nm. The thickness of the hollow-SiO_2 shell was 45±5 nm. Through etching of s/h SiO_2 NPs using Na_2CO_3 solution, rattle-type SiO_2 was successfully formed, as shown in **Figure S9** and **Figure 2**a, the large mesoporous channels in the outer shells were visualized clearly. Meanwhile, r-SiO_2 was modified with polyethylenimine (PEI) in order to form the MISO armored r-SiO_2 composite nanoparticles. The successful synthesis of SMISO NPs was evidenced by zeta potential analysis (**Figure S10**), SEM and TEM examinations (**Figure S11a-b** and Figure 2b). The PEI modification induces the change of SiO_2 surface charge from negative to positive; after loading of MISO, the zeta potential changes from +25.5 mV to +20.3 mV, indicating successful anchoring of MISO on SiO_2. MISO NPs are homogenously and densely dispersed over the surface of SiO_2, and SMISO NPs present homogeneous shape and relatively uniform size as shown in **Figure S11** and Figure 2b. The energy-dispersive spectroscopy element mapping (Figure S12) reveals the distributions of In and S elements in the SMISO composite NPs. The XRD analysis shows that the peaks of SMISO NPs are well-corresponded with the SiO_2 (amorphous phase), β-In_2S_3 and InOOH patterns (Figure 3c). The chemical composition of SMISO NPs was further confirmed from the X-ray photoelectron spectra (**Figure S13**), whereby the deconvoluted In 3d peaks located at 452 eV and 444.5 eV corresponded to In $3d_{3/2}$ and In $3d_{5/2}$ orbitals of In(III), respectively. The deconvoluted S 2p peaks located at 161 eV and 162.2eV with a doublet

separation of 1.2 eV were assigned to the S $2p_{3/2}$ and S $2p_{1/2}$ orbitals of divalent sulfide (S^{2-}), respectively.[34] In the SDT performance test, SMISO NPs exhibited a higher DPBF oxidation rate under acid conditions (pH = 5.5) than that under neutral conditions (pH = 7.4) (Figure 2d). This was attributed to the release of MISO from SMISO and the exposure of the active sites, as shown in **Figure S14 and Figure S15**.

In the previous studies, SiO_2 NPs have been investigated as gas-free ultrasound contrast agents and have been demonstrated to allow ultrasound imaging.[35] In our study, acoustic reflection and scattering signals of SiO_2, MISO and SMISO were measured and compared. While the squared amplitude of ultrasound is positively proportional to the averaged gray value of *in vitro* ultrasound images (Figure 2e-f),[17] the reflection and scattering ratios of r-SiO_2 to s/h SiO_2 are 1.95 and 1.10, respectively, calculated from their ultrasound signal intensity. This indicates that the increased imaging capacity of r-SiO_2 is attributed to the promoted reflection. MISO NPs have a medium reflection signal and a strong scattering signal. The reflection and scattering ratios of SMISO to r-SiO_2 are 1.80 and 1.88, respectively, confirming the optimal imaging performance of the composite. Ultrasound B fundamental imaging mode was employed to test the imaging capacity of the above materials, with both reflection and scattering signals contributing to the ultrasound imaging, although the scattering signal is the major contributor.[17] As shown in Figure 2g and **Figure S16**a, SMISO NPs exhibit excellent and enhanced ultrasound imaging capacity than the other three materials. The gray value of US images of SMISO NPs increases with their concentrations (Figure S16b-c). To understand the mechanism of efficient ultrasound imaging of SMISO NPs, r-SiO_2 with different etching times were synthesized. The diameter of the core was decreased time-dependently, as shown in **Figure S17** and Figure 2a. The reflection signals of the etched r-SiO_2 varied with different etching time, and the NPs etched for 1 hour exhibited the best

reflection performance, with the variation of scattering signals being relatively small (**Figure S18**). This phenomenon could be due to multiple reflection/scattering occurred from shell-medium and medium-core interfaces in 1h etched r-SiO_2, while limited reflection/scattering of ultrasound from the s/h SiO_2 surfaces of particles etched of 0 h and 0.5 h. The inner core size decreased as with the etch time increased to 3 h, but scattering cross-interfaces decreased. The quality of *in vitro* ultrasound imaging was correlated to the levels of reflection/scattering at the interfaces (**Figure S19**). Therefore, a proposed mechanism of ultrasound imaging of SMISO NPs is summarized in Figure 2h. The structural design of r-SiO_2 with multiple interfaces induces further reflection/scattering after ultrasound irradiation.[17, 36] The incident waves could be reflected and scattered by the 1st shell-medium layer interface and the transmitted wave could be reflected and scattered by the 2nd medium-core interface, thus enhanced reflection and scattering occurs twice in one nanoparticle and increased imaging contrast can be achieved. As reflection relies on the density and acoustic impedance of materials, MISO NPs anchored on the surface of SiO_2, which have high acoustic impedance, can further promote the reflection intensity and facilitate ultrasound imaging.

3.2. *In vitro* study

Next, the *in vitro* SDT effect induced by SMISO NPs was evaluated by the standard methyl thiazolyl tetrazolium (MTT) assay using the 4T1 mouse breast cancer cell line. As shown in **Figure 3**a, SMISO NPs show good cytocompatibility over the given concentration range (25-200 μg mL^{-1}) after co-incubation for 24 h. The cell viability significantly declined under US irradiation (1.0 MHz, 1.0 W cm^{-2}, 3 min), whereby only 17% of cells survived at the concentration of 200 μg mL^{-1}. As a comparison, SiO_2 and MISO NPs exhibited no clear toxicity to 4T1 cells (Figure 3b). When exposed to US, SiO_2 NPs exhibited weak sono-killing effect due to the relative mechanical motion

of nanoparticles ('nanoscalpel effect'), as previously reported.[37] MISO NPs showed a similar cytotoxicity to SMISO NPs under US irradiation, which is attributed to the pH-responsive release of MISO from SMISO in the cell culture environment. Furthermore, the cell death derived from SMISO-mediated SDT was investigated qualitatively by fluorescence microscopy and quantitatively by flow cytometry. The Annexin V-fluorescein isothiocyanate (FITC) and propidium iodide (PI) double staining test verified that the majority of cells were killed when cultured with MISO or SMISO NPs under US irradiation, confirming their excellent SDT efficiency (Figure 3d-e). To confirm the cell viability, calcein-AM (green, staining live cells) and PI (red, staining dead cells) were co-incubated with cells after different treatments using SiO_2, MISO and SMISO with or without US irradiation (Figure 3f). The groups of MISO + US and SMISO + US showed strong red fluorescence, indicating that these two groups induced significant damage to 4T1 cells. To further validate the therapeutic mechanism of SMISO NPs as a sonosensitizer, the intracellular ROS generation was analyzed using 2,7-dichlorofluorescein diacetate (DCFH-DA) staining assay qualitatively and quantitatively. After penetrating the cells, DCFH-DA could be hydrolyzed by esterase and subsequently oxidized by ROS to produce DCFH, which emits green fluorescence under blue light. A distinct increase of ROS levels was noticed when combining MISO or SMISO with US irradiation (Figure 3c, **Figure S20 and Table S1**), whereas no clear change was detected in the control group and in the cells treated with SiO_2, MISO, SMISO and US alone, demonstrating a significant SDT effect of MISO and SMISO. Moreover, an enhancement of fluorescence intensity in SiO_2 + US group confirmed the nanoscalpel effect of SiO_2, which can promote the intracellular ROS generation (Figure 3f).

3.3. *In vivo* ultrasound imaging and antitumor study

A real-time B mode US imaging *in vivo* which is based on the change of gray scale at the region of interest was assessed in the 4T1 breast cancer model. Normal saline, SiO_2, MISO and SMISO solutions were intratumorally injected into the tumor site at the tumor-bearing nude mice and the change of gray scale was detected subsequently. It could be clearly observed that there were pronounced changes of gray scale after treated with SiO_2, MISO or SMISO solutions. A significant difference of gray value ($p < 0.01$) existed between SMISO and the control group (**Figure 4a** and 4c), which confirmed that SMISO NPs have a great potential to be an ultrasound contrast agent. Furthermore, SMISO NPs were intravenously (i.v.) injected into the tail vein of 4T1 tumor-bearing nude mice and the tumor site was scanned at each time period. As evidenced from the ultrasound images (Figure 4b) and quantitative comparison of the signal intensity (Figure 4d) following the injection from 0 to 24 h, the signal intensity from the tumor site increased gradually and peaked at 12 h. This phenomenon can be ascribed to a time-dependent accumulation of SMISO NPs at the tumor site through the enhanced permeability and retention (EPR) effect. As the circulation time was further prolonged, SMISO NPs were broken down and metabolized out of the tumor. These results confirm the ultrasound imaging capacity of SMISO NPs, while also providing guidance as to the optimal exposure timing for US irradiation so as to facilitate the subsequent treatment *in vivo*.

Encouraged by the ultrasound-mediated antitumor activity and ultrasound imaging guidance of SMISO NPs, *in vivo* experiments were conducted on mice with 4T1 tumors; a methodological flowchart is shown in **Figure 5**a. The 4T1 tumor-bearing mice were equally and randomly divided into six groups (n = 5): (1) Control (normal saline, i.v. injection), (2) US alone (1.0 MHz, 1.5 W cm^{-2}, 2 min), (3) SiO_2 + US (10 mg kg^{-1}, i.v. injection), (4) MISO + US (5 mg kg^{-1}, i.v. injection), (5) SMISO alone (15 mg kg^{-1}, i.v. injection), (6) SMISO + US (15 mg kg^{-1}, i.v. injection). At 12 h

and 24 h post intravenous (i.v.) injection of the above materials, the tumor sites were subjected to US irradiation and the administration was repeated three times during the 15 days' treatment period (every 5 days). The body weight and the tumor volume of each mouse were monitored every two days. As shown in **Figure S21-23**, no pronounced abnormalities of body weight occurred, implying that the treatment protocols are safe for biological applications. After the treatment, the inhibition rate of tumor growth in SMISO + US group reached to 88.2%, which is significantly higher than the other groups (Figure 5b and **Figure S24**). The variations of tumor weights and the representative photographs of tumors dissected at the end of treatment also verified the best SDT efficiency of SMISO NPs (Figure 5c-d). Notably, the therapeutic effect of MISO +US group is weak, which could be ascribed to the rapid clearance of small-size MISO NPs in the mouse. The exceptional therapeutic effect of SMISO NPs was further investigated by H&E and Ki67 staining of tumors slices (Figure 5e). H&E staining images of the cross sections were compared with the other five groups, and showed that the tumor tissues in SMISO + US group exhibit typical apoptotic characteristics, including numerous nuclear pyknosis and severe cytoplasmic vacuolization. Ki67 staining results demonstrate that the treatment with SMISO and US irradiation substantially induced Ki67-positive cells and the proliferation of 4T1 cells was significantly inhibited, which corresponds well with the *in vivo* study. In addition, ROS staining of tumor tissue was carried out using dihydroethidium (DHE) to assess the production of ROS after different treatments (Figure 5f). It is clear that SMISO + US group showed the strongest red fluorescence compared with other groups. This finding implies the highest ROS level generated from SMISO NPs and confirms the excellent SDT performance of SMISO NPs. To study the biosafety of SMISO NPs, the body clearance behavior of SMISO NPs was investigated by measuring the accumulation of materials in the main organs (heart, liver, spleen, kidney and tumor) at different

time points post i.v. injection using inductively coupled plasma optical emission spectra (ICP-OES) (**Figure 6**a). Over a period of 24 h, the retention of SMISO NPs mainly presented at liver, spleen, lung and tumor. While at 72 h post injection, the distribution in these organs decreased due to the metabolism and clearance out of the body. Additionally, at 1st, 3rd and 7th days after i.v. injection of SMISO NPs, the blood biochemistry and hematologic analysis were conducted to verify the systemic toxicity of SMISO NPs (Figure 6b-l). No abnormalities and obvious side effects to the animals were found from all the main biochemical indices, including alanine aminotransferase (ALT), aspartate aminotransferase (AST), total bilirubin (TBIL), white blood cell (WBC), red blood cell (RBC), blood platelet (PLT), hematocrit (HCT), hemoglobin (HGB), mean corpuscular volume (MCV), mean corpuscular hemoglobin concentration (MCHC) and mean corpuscular hemoglobin (MCH). H&E staining of the main organs (heart, liver, spleen, lung and kidney) that were dissected at the end of the treatment were presented in Figure 6m and **Figure S25.** The results show that SMISO NPs did not present clear negative effects to the main organs, demonstrating the non-toxicity nature of SMISO NPs for its potential applications.

4. Conclusions

In summary, we have successfully synthesized a novel theranostic system of SMISO nanoparticles which enables simultaneous ultrasound imaging and sonodynamic therapy for tumor inhibition. Following the reflection/scattering occurring on the liquid-solid interface, the compounding of rattle-type SiO_2 with multi-reflection/scattering interfaces and high acoustic impedance of MISO shows an outstanding ultrasound imaging performance. Using B-mode ultrasound medical imaging, the SMISO composite nanoparticles can serve as an ultrasound contrast agent to detect the tumor growth and realize imaging-guided SDT. Besides, through combining In_2S_3 with InOOH and Mn doping, the new type of sonosensitizer MISO can effectively facilitate the separation of

activated electrons and holes for the US-induced ROS generation. Under US irradiation, SMISO NPs exhibit an excellent pH-responsive ROS generation capability and an effective killing of tumor cells. The *in vivo* results demonstrate that SMISO NPs have an excellent biosafety and superior suppressive effects on the proliferation of tumor cells, thus effectively inhibiting the tumor growth without harming to the body. Therefore, this innovative design of SMISO paves a new way to develop ultrasound contrast agents and sonosensitizers in ultrasonic tumor therapy.

ASSOCIATED CONTENT

Supporting Information.

The supporting information is available free of charge.

TEM images of 0-MISO and 5-MISO; The mass ratio of Mn versus In in 0-MISO, 1-MISO and 5-MISO; DPBF degradation curve (with and without US irradiation), UV-visible diffuse reflectance spectra of 0-MISO, 1-MISO and 5-MISO; ESR measurements; The chemodynamic effect of MISO; SEM and TEM images of s/h SiO_2; SEM images of rattle-type SiO_2; Zeta potentials; SEM images, low-magnification TEM image, EDS element mapping and XPS spectra of SMISO; SEM and TEM images of SMISO upon acid treatment; *In vitro* US images; reflection and scattering signals of SiO_2; ROS fluorescence intensity and the quantification data; Body weight variation; The original tumor volume variation; Representative mice photographs; Tumor inhibition rate; H&E staining images. (DOC)

AUTHOR INFORMATION

Corresponding Author

Yike Fu − State Key Laboratory of Silicon Materials, School of Materials Science and Engineering, Zhejiang University, Hangzhou, Zhejiang 310027, P. R. China; ZJU-Hangzhou Global Scientific and Technological Innovation Center, Zhejiang University, Hangzhou, 311200, P.R. China. Email: fyk3927@zju.edu.cn.

Xiujun Cai − Key Laboratory of Endoscopic Technique Research of Zhejiang Province, Sir Run Run Shaw Hospital, Zhejiang University, Hangzhou 215123, P. R. China. Email: srrsh_cxj@zju.edu.cn.

Xiang Li − State Key Laboratory of Silicon Materials, School of Materials Science and Engineering, Zhejiang University, Hangzhou, Zhejiang 310027, P. R. China; ZJU-Hangzhou Global Scientific and Technological Innovation Center, Zhejiang University, Hangzhou, 311200, P.R. China. Email: xiang.li@zju.edu.cn (XL).

Authors

Tian Zhang − State Key Laboratory of Silicon Materials, School of Materials Science and Engineering, Zhejiang University, Hangzhou, Zhejiang 310027, P. R. China.

Qiang Zheng − Key Laboratory of Endoscopic Technique Research of Zhejiang Province, Sir Run Run Shaw Hospital, Zhejiang University, Hangzhou 215123, P. R. China.

Congkun Xie − State Key Laboratory of Silicon Materials, School of Materials Science and Engineering, Zhejiang University, Hangzhou, Zhejiang 310027, P. R. China.

Gonglin Fan − Key Laboratory of Endoscopic Technique Research of Zhejiang Province, Sir Run Run Shaw Hospital, Zhejiang University, Hangzhou 215123, P. R. China.

Yifan Wang − Key Laboratory of Endoscopic Technique Research of Zhejiang Province, Sir Run Run Shaw Hospital, Zhejiang University, Hangzhou 215123, P. R. China.

Yongjun Wu − State Key Laboratory of Silicon Materials, School of Materials Science and Engineering, Zhejiang University, Hangzhou, Zhejiang 310027, P. R. China.

Jie Huang − Department of Mechanical Engineering, University College London, London WC1E 7JE, UK.

Duncan Q.M. Craig − University College London School of Pharmacy, London WC1N 1AX, UK

Author Contributions

Tian Zhang: Investigation, Methodology, Writing – original draft. Qiang Zheng: Investigation, Methodology. Congkun Xie: Methodology. Gonglin Fan: Methodology. Yifan Wang: Data curation. Yongjun Wu: Funding acquisition, Supervision. Yike Fu: Data curation, Writing - review & editing. Jie Huang: Funding acquisition, Supervision. Duncan Q.M. Craig: Writing - review & editing, Supervision. Xiujun Cai: Project administration, Funding acquisition. Xiang Li: Conceptualization, Writing - review & editing, Supervision.

Funding Sources

National Nature Science Foundation of China (52172289, 51902288), Provincial Key Research Program of Zhejiang Province (2020C04005), and Fundamental Research Funds for the Central Universities.

Notes

The authors declare no conflict of interest.

ACKNOWLEDGMENT

This work was financially supported by National Nature Science Foundation of China (52172289, 51902288), Provincial Key Research Program of Zhejiang Province (2020C04005), and Fundamental Research Funds for the Central Universities.

REFERENCES

(1) Nuevo-Tapioles, C.; Santacatterina, F.; Stamatakis, K.; Nunez de Arenas, C.; Gomez de Cedron, M.; Formentini, L.; Cuezva, J. M. Coordinate Beta-Adrenergic Inhibition of Mitochondrial Activity and Angiogenesis Arrest Tumor Growth. *Nature Communications* **2020**, *11* (1), 3606.

(2) Wang, Y.; Yang, T.; He, Q. Strategies for Engineering Advanced Nanomedicines for Gas Therapy of Cancer. *National Science Review* **2020**, *7* (9), 1485-1512.

(3) Lin, H.; Chen, Y.; Shi, J. Insights into 2d Mxenes for Versatile Biomedical Applications: Current Advances and Challenges Ahead. *Advanced Science* **2018**, *5* (10), 1800518.

(4) Qu, F.; Wang, P.; Zhang, K.; Shi, Y.; Li, Y.; Li, C.; Lu, J.; Liu, Q.; Wang, X. Manipulation of Mitophagy by "All-in-One" Nanosensitizer Augments Sonodynamic Glioma Therapy. *Autophagy* **2020**, *16* (8), 1413-1435.

(5) Yao, J.; Yang, Z.; Huang, L.; Yang, C.; Wang, J.; Cao, Y.; Hao, L.; Zhang, L.; Zhang, J.; Li, P.; Wang, Z.; Sun, Y.; Ran, H. Low-Intensity Focused Ultrasound-Responsive Ferrite-Encapsulated Nanoparticles for Atherosclerotic Plaque Neovascularization Theranostics. *Advanced Science* **2021**, *8* (19), 2100850.

(6) Zhang, T.; Zheng, Q.; Fu, Y.; Xie, C.; Fan, G.; Wang, Y.; Wu, Y.; Cai, X.; Han, G.; Li, X. Alpha-Fe_2O_3@Pt Heterostructure Particles to Enable Sonodynamic Therapy with Self-Supplied O-2 and Imaging-Guidance. *Journal Of Nanobiotechnology* **2021**, *19* (1), 358.

(7) Wu, J.; Williams, G. R.; Niu, S.; Gao, F.; Tang, R.; Zhu, L.-M. A Multifunctional Biodegradable Nanocomposite for Cancer Theranostics. *Advanced Science* **2019**, *6* (14), 1802001.

(8) Lakshmanan, A.; Lu, G. J.; Farhadi, A.; Nety, S. P.; Kunth, M.; Lee-Gosselin, A.; Maresca, D.; Bourdeau, R. W.; Yin, M.; Yan, J.; Witte, C.; Malounda, D.; Foster, F. S.; Schroeder, L.; Shapiro, M. G. Preparation of Biogenic Gas Vesicle Nanostructures for Use as Contrast Agents for Ultrasound and Mri. *Nature Protocols* **2017**, *12* (10), 2050-2080.

(9) Ozdas, M. S.; Shah, A. S.; Johnson, P. M.; Patel, N.; Marks, M.; Yasar, T. B.; Stalder, U.; Bigler, L.; von der Behrens, W.; Sirsi, S. R.; Yanik, M. F. Non-Invasive Molecularly-Specific Millimeter-Resolution Manipulation of Brain Circuits by Ultrasound-Mediated Aggregation and Uncaging of Drug Carriers. *Nature Communications* **2020**, *11* (1), 4929.

(10) Duan, L.; Yang, L.; Jin, J.; Yang, F.; Liu, D.; Hu, K.; Wang, Q.; Yue, Y.; Gu, N. Micro/Nano-Bubble-Assisted Ultrasound to Enhance the EPR Effect and Potential Theranostic Applications. *Theranostics* **2020**, *10* (2), 462-483.

(11) Delaney, L. J.; Eisenbrey, J. R.; Brown, D.; Brody, J. R.; Jimbo, M.; Oeffinger, B. E.; Stanczak, M.; Forsberg, F.; Liu, J.-B.; Wheatley, M. A. Gemcitabine-Loaded Microbubble System for Ultrasound Imaging and Therapy. *Acta Biomaterialia* **2021**, *130*, 385-394.

(12) Jones, R. M.; McMahon, D.; Hynynen, K. Ultrafast Three-Dimensional Microbubble Imaging in Vivo Predicts Tissue Damage Volume Distributions During Nonthermal Brain Ablation. *Theranostics* **2020**, *10* (16), 7211-7230.

(13) Zhang, L.; Yi, H.; Song, J.; Huang, J.; Yang, K.; Tan, B.; Wang, D.; Yang, N.; Wang, Z.; Li, X. Mitochondria-Targeted and Ultrasound-Activated Nanodroplets for Enhanced Deep-Penetration Sonodynamic Cancer Therapy. *Acs Applied Materials & Interfaces* **2019**, *11* (9), 9355-9366.

(14) Li, M.; Bian, X.; Chen, X.; Fan, N.; Zou, H.; Bao, Y.; Zhou, Y. Multifunctional Liposome for Photoacoustic/Ultrasound Imaging-Guided Chemo/Photothermal Retinoblastoma Therapy. *Drug delivery* **2022**, *29* (1), 519-533.

(15) Lu, N.; Fan, W.; Yi, X.; Wang, S.; Wang, Z.; Tian, R.; Jacobson, O.; Liu, Y.; Yung, B. C.; Zhang, G.; Teng, Z.; Yang, K.; Zhang, M.; Niu, G.; Lu, G.; Chen, X. Biodegradable Hollow Mesoporous Organosilica Nanotheranostics for Mild Hyperthermia-Induced Bubble-Enhanced Oxygen-Sensitized Radiotherapy. *Acs Nano* **2018**, *12* (2), 1580-1591.

(16) Deng, L.; Cai, X.; Sheng, D.; Yang, Y.; Strohm, E. M.; Wang, Z.; Ran, H.; Wang, D.; Zheng, Y.; Li, P.; Shang, T.; Ling, Y.; Wang, F.; Sun, Y. A Laser-Activated Biocompatible Theranostic Nanoagent for Targeted Multimodal Imaging and Photothermal Therapy. *Theranostics* **2017**, *7* (18), 4410-4423.

(17) Zhang, K.; Chen, H.; Guo, X.; Zhang, D.; Zheng, Y.; Zheng, H.; Shi, J. Double-Scattering/Reflection in a Single Nanoparticle for Intensified Ultrasound Imaging. *Scientific Reports* **2015**, *5*, 8766.

(18) Meng, X.; Yi, Y.; Meng, Y.; Lv, G.; Jiang, X.; Wu, Y.; Yang, W.; Yao, Y.; Xu, H.; Bu, W. Self-Enhanced Acoustic Impedance Difference Strategy for Detecting the Acidic Tumor Microenvironment. *Acs Nano* **2022**, *16* (3), 4217-4227.

(19) Yue, W.; Chen, L.; Yu, L.; Zhou, B.; Yin, H.; Ren, W.; Liu, C.; Guo, L.; Zhang, Y.; Sun, L.; Zhang, K.; Xu, H.; Chen, Y. Checkpoint Blockade and Nanosonosensitizer- Augmented Noninvasive Sonodynamic Therapy Combination Reduces Tumour Growth and Metastases in Mice. *Nature Communications* **2019**, *10*, 2025.

(20) Zhang, C.; Huang, J.; Zeng, Z.; He, S.; Cheng, P.; Li, J.; Pu, K. Catalytical Nano-Immunocomplexes for Remote-Controlled Sono-Metabolic Checkpoint Trimodal Cancer Therapy. *Nature Communications* **2022**, *13* (1), 3468.

(21) Xu, W.; Dong, C.; Hu, H.; Qian, X.; Chang, L.; Jiang, Q.; Yu, L.; Chen, Y.; Zhou, J. Engineering Janus Chemoreactive Nanosonosensitizers for Bilaterally Augmented Sonodynamic and Chemodynamic Cancer Nanotherapy. *Advanced Functional Materials* **2021**, *31* (37), 2103134.

(22) Liang, S.; Deng, X.; Ma, P. a.; Cheng, Z.; Lin, J. Recent Advances in Nanomaterial-Assisted Combinational Sonodynamic Cancer Therapy. *Advanced Materials* **2020**, *32* (47), 2003214.

(23) Li, J.; Luo, Y.; Zeng, Z.; Cui, D.; Huang, J.; Xu, C.; Li, L.; Pu, K.; Zhang, R. Precision Cancer Sono-Immunotherapy Using Deep-Tissue Activatable Semiconducting Polymer Immunomodulatory Nanoparticles. *Nature communications* **2022**, *13* (1), 4032-4032.

(24) Chowdhury, F. A.; Trudeau, M. L.; Guo, H.; Mi, Z. A Photochemical Diode Artificial Photosynthesis System for Unassisted High Efficiency Overall Pure Water Splitting. *Nature Communications* **2018**, *9*, 1707.

(25) Zeng, Z.; Zhang, C.; He, S.; Li, J.; Pu, K. Activatable Cancer Sono-Immunotherapy Using Semiconducting Polymer Nanobodies. *Advanced Materials* **2022**, *34* (28), 2203246.

(26) Senkovskiy, B. V.; Nenashev, A. V.; Alavi, S. K.; Falke, Y.; Hell, M.; Bampoulis, P.; Rybkovskiy, D. V.; Usachov, D. Y.; Fedorov, A. V.; Chernov, A. I.; Gebhard, F.; Meerholz, K.; Hertel, D.; Arita, M.; Okuda, T.; Miyamoto, K.; Shimada, K.; Fischer, F. R.; Michely, T.; Baranovskii, S. D.; Lindfors, K.; Szkopek, T.; Grueneis, A. Tunneling Current Modulation in Atomically Precise Graphene Nanoribbon Heterojunctions. *Nature Communications* **2021**, *12* (1), 2542.

(27) Bai, S.; Yang, N.; Wang, X.; Gong, F.; Dong, Z.; Gong, Y.; Liu, Z.; Cheng, L. Ultrasmall Iron-Doped Titanium Oxide Nanodots for Enhanced Sonodynamic and Chemodynamic Cancer Therapy. *Acs Nano* **2020**, *14* (11), 15119-15130.

(28) Liang, S.; Xiao, X.; Bai, L.; Liu, B.; Yuan, M.; Ma, P. a.; Pang, M.; Cheng, Z.; Lin, J. Conferring Ti-Based MOFs with Defects for Enhanced Sonodynamic Cancer Therapy. *Advanced Materials* **2021**, *33* (18), 2100333.

(29) Liu, Y.; Yu, B.; Dai, X.; Zhao, N.; Xu, F.-J. Biomineralized Calcium Carbonate Nanohybrids for Mild Photothermal Heating-Enhanced Gene Therapy. *Biomaterials* **2021**, *274*, 120885.

(30) Pan, X.; Wang, W.; Huang, Z.; Liu, S.; Guo, J.; Zhang, F.; Yuan, H.; Li, X.; Liu, F.; Liu, H. MOF-Derived Double-Layer Hollow Nanoparticles with Oxygen Generation Ability for Multimodal Imaging-Guided Sonodynamic Therapy. *Angewandte Chemie-International Edition* **2020**, *59* (32), 13557-13561.

(31) Wang, X.; Liu, W.; Wang, X.; Yu, D.; Liu, H. Preparation of In_2S_3@TiO_2 Nanobelt Heterostructures with High UV-Visible Light Photocatalytic Activities. *Science of Advanced Materials* **2015**, *7* (3), 479-488.

(32) Fan, Z.; Yuan-Yuan, Z.; Ya-Sai, S.; Run-Hui, M.; Kiran, T.; Jian-Guo, Z.; Zhao-Jun, W. Asparanin a from Asparagus Officinalis L. Induces G0/G1 Cell Cycle Arrest and Apoptosis in Human Endometrial Carcinoma Ishikawa Cells Via Mitochondrial and PI3k/AKT Signaling Pathways. *Journal of Agricultural and Food Chemistry* **2020**, *68* (1), 213-224.

(33) Ghini, M.; Curreli, N.; Lodi, M. B.; Petrini, N.; Wang, M.; Prato, M.; Fanti, A.; Manna, L.; Kriegel, I. Control of Electronic Band Profiles through Depletion Layer Engineering in Core-Shell Nanocrystals. *Nature Communications* **2022**, *13* (1), 537.

(34) Wu, Z.; Yuan, X.; Zeng, G.; Jiang, L.; Zhong, H.; Xie, Y.; Wang, H.; Chen, X.; Wang, H. Highly Efficient Photocatalytic Activity and Mechanism of Yb^{3+}/Tm^{3+} Codoped In_2S_3 from Ultraviolet to near Infrared Light Towards Chromium (Vi) Reduction and Rhodamine B Oxydative Degradation. *Applied Catalysis B-Environmental* **2018**, *225*, 8-21.

(35) Lin, P.-L.; Eckersley, R. J.; Hall, E. A. H. Ultrabubble: A Laminated Ultrasound Contrast Agent with Narrow Size Range. *Advanced Materials* **2009**, *21* (38-39), 3949-+.

(36) Yang, P.; Wang, F.; Luo, X.; Zhang, Y.; Guo, J.; Sho, W.; Wang, C. Rational Design of Magnetic Nanorattles as Contrast Agents for Ultrasound/Magnetic Resonance Dual-Modality Imaging. *Acs Applied Materials & Interfaces* **2014**, *6* (15), 12581-12587.

(37) Osminkina, L. A.; Nikolaev, A. L.; Sviridov, A. P.; Andronova, N. V.; Tamarov, K. P.; Gongalsky, M. B.; Kudryavtsev, A. A.; Treshalina, H. M.; Timoshenko, V. Y. Porous Silicon Nanoparticles as Efficient Sensitizers for Sonodynamic Therapy of Cancer. *Microporous and Mesoporous Materials* **2015**, *210*, 169-175.

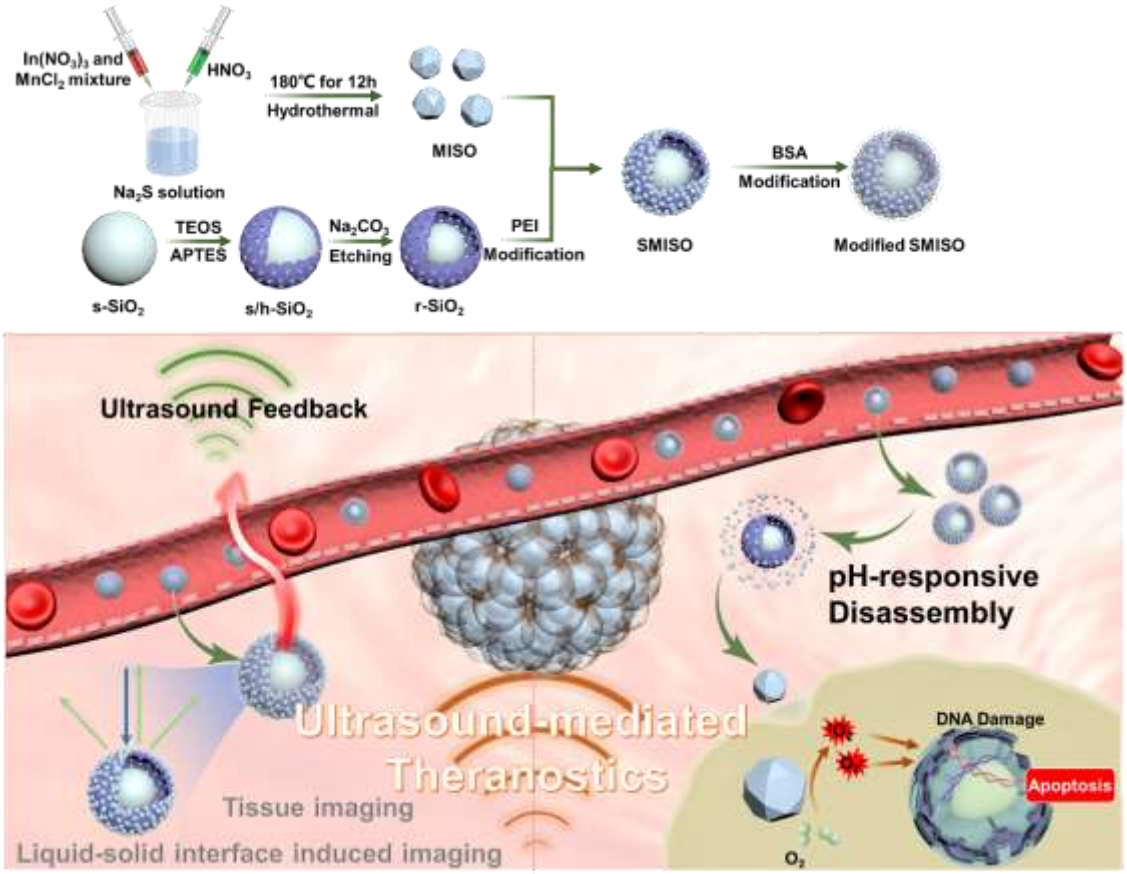

Scheme 1. Schematic illustration of the synthesis process of SMISO NPs and their application for theranostics: a double agent (a) an ultrasound contrast agent (UCA) and (b) sonosensitizer for sonodynamic therapy (SDT).

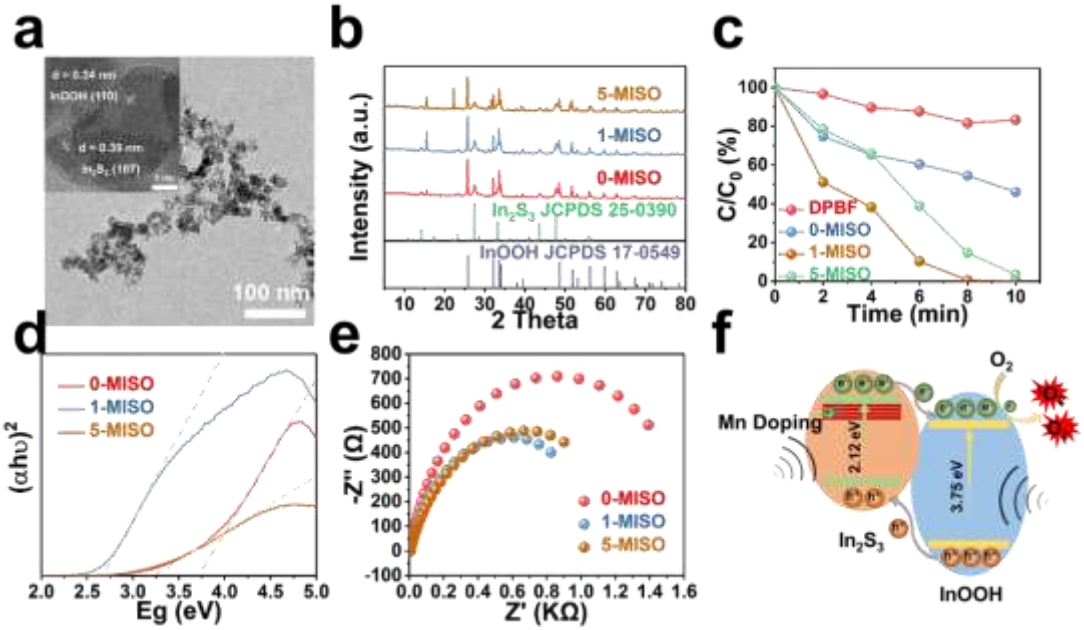

Figure 1. (a) TEM image of 1-MISO nanoparticles. Inset: High-resolution TEM image. (b) XRD patterns of MISO with 0, 1 and 5% Mn doping (0-MISO, 1-MISO and 5-MISO). (c) Normalized absorbance of DPBF after incubated with/without MISO with Mn dopings under the US irradiation (1.0 MHz, 1.0 W cm^{-2}) for 0 to 10 mins. (d) The relationship between $(\alpha h\nu)^2$ versus *Eg* of 0-MISO, 1-MISO and 5-MISO. (e) Nyquist plots of 0-MISO, 1-MISO and 5-MISO from EIS measurement. (f) A proposed SDT mechanism of MISO NPs under US irradiation.

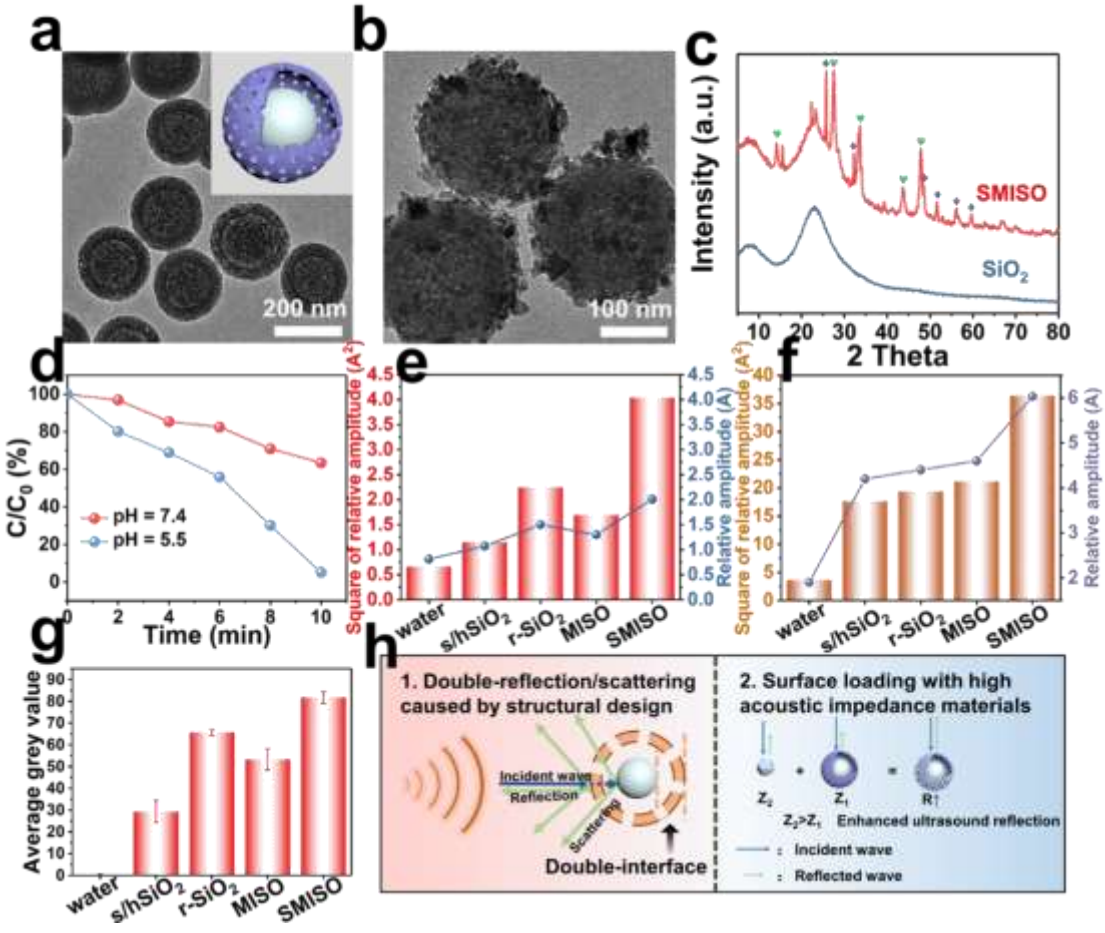

Figure 2. Characteristics and intrinsic properties of SMISO. TEM images of (a) Rattle-type SiO_2 and (b) SMISO NPs. (c) XRD patterns of rattle-type SiO_2 and SMISO NPs. (d) SDT performance of SMISO under neutral (pH = 7.4) and acid (pH = 5.5) conditions. The relative echo amplitudes (A and A^2) of (e) the reflected sound waves and (f) the scattering signals of the test solutions, including water, s/h SiO_2, r-SiO_2, MISO and SMISO. (g) Comparison of measured average gray value of US imaging for the test solutions *in vitro*. (h) Schematic illustration of the US imaging mechanism of SMISO NPs.

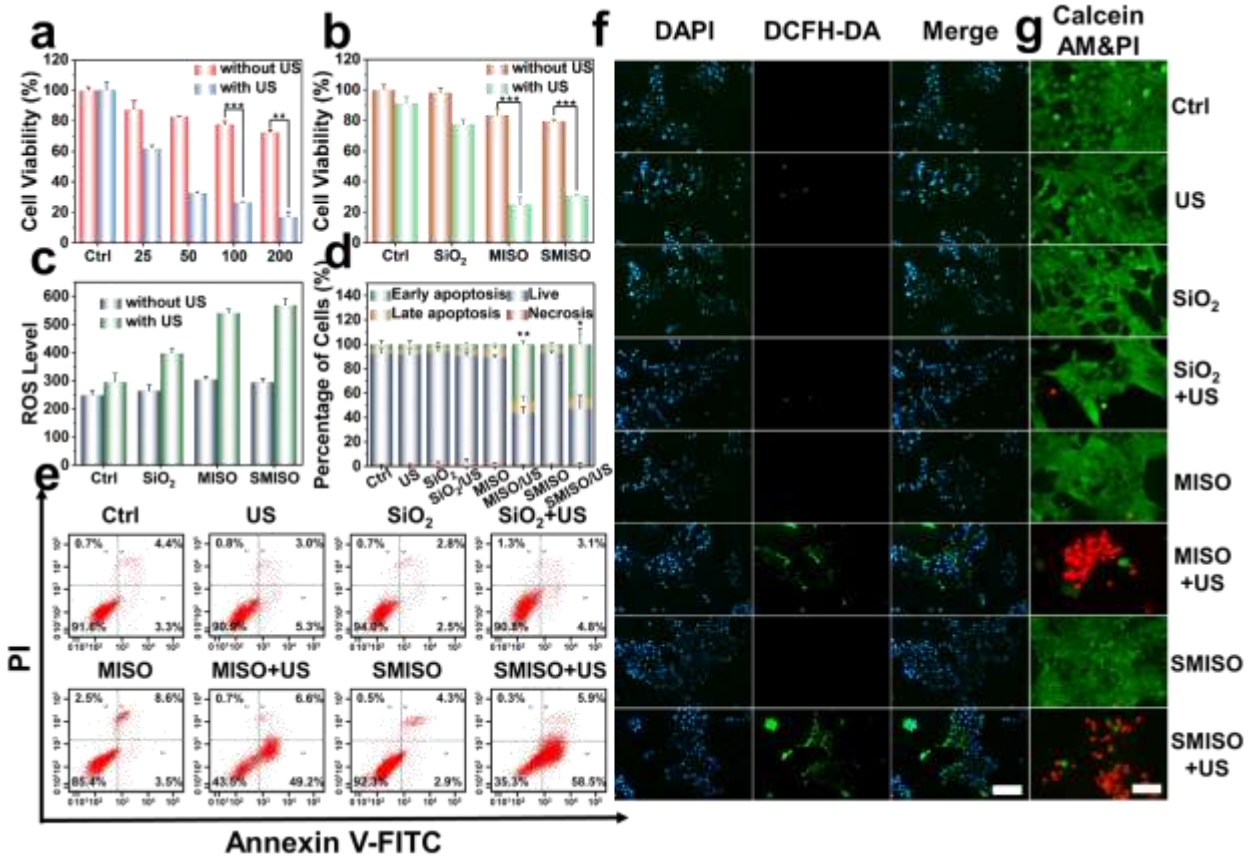

Figure 3. *In vitro* SDT performance of SMISO NPs. (a) Relative cell viability of 4T1 cells incubated with the concentrations of SMISO (0-200 μg mL^{-1}) for 24 h in the presence or absence of US (1.0 MHz, 1.0 W cm^{-2}, 3 min). (b) Relative cell viability of 4T1 cells incubated with the solutions containing SiO_2, MISO and SMISO with or without US irradiation. (c) Quantitative analysis by flow cytometer of the ROS levels after the treatments combining with SiO_2, MISO and SMISO. (d) Corresponding quantitative analysis and (e) flow cytometry of 4T1 cell apoptosis staining with PI and Annexin V-FITC under the different treatments. (f) Fluorescence images of 4T1 cells stained with DAPI, DCFH-DA under different treatments. Scale bar: 200 μm. (g) Fluorescence images of 4T1 cells stained with Calcein AM and PI under different treatments. Scale bar: 100 μm. *** $p < 0.001$, ** $p < 0.01$ and * $p < 0.05$.

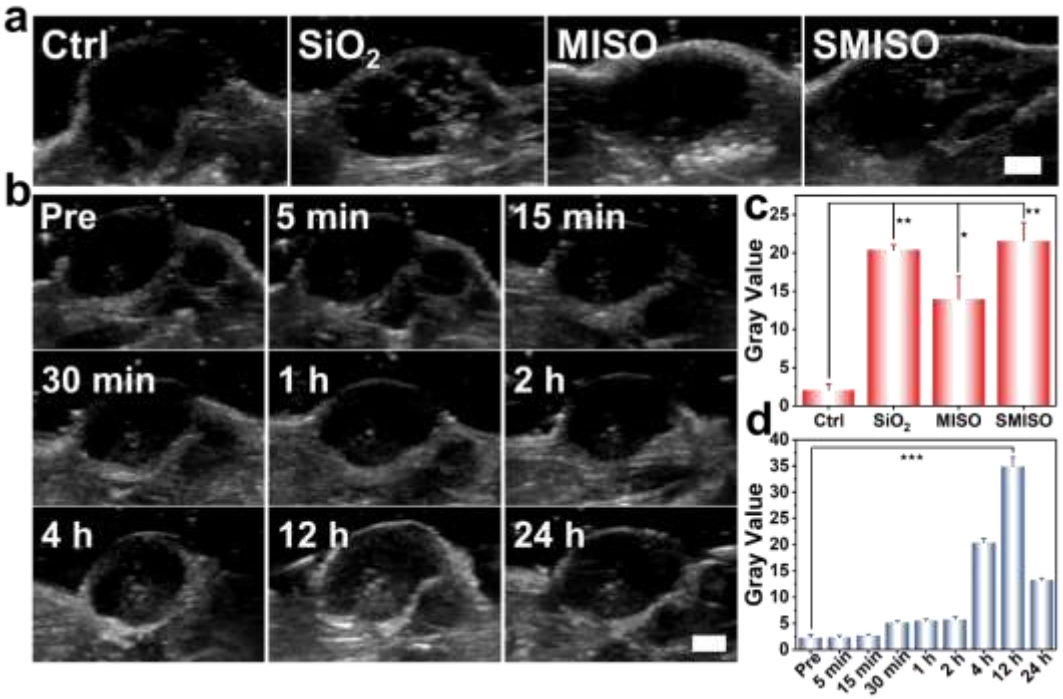

Figure 4. *In vivo* B-mode US imaging performed in 4T1 tumor-bearing nude mice. (a) US images and (c) corresponding gray value of tumors obtained 5 min after intratumoral injection with PBS, SiO_2 (10 mg kg^{-1}), MISO (5 mg kg^{-1}), and SMISO (15 mg kg^{-1}). Scale bar: 2 mm. (b) US images and (d) corresponding gray value of tumors obtained at various time points (0-24 h) after intravenous injection with SMISO (15 mg kg^{-1}). Scale bar: 2 mm. *** $p < 0.001$, ** $p < 0.01$ and * $p < 0.05$.

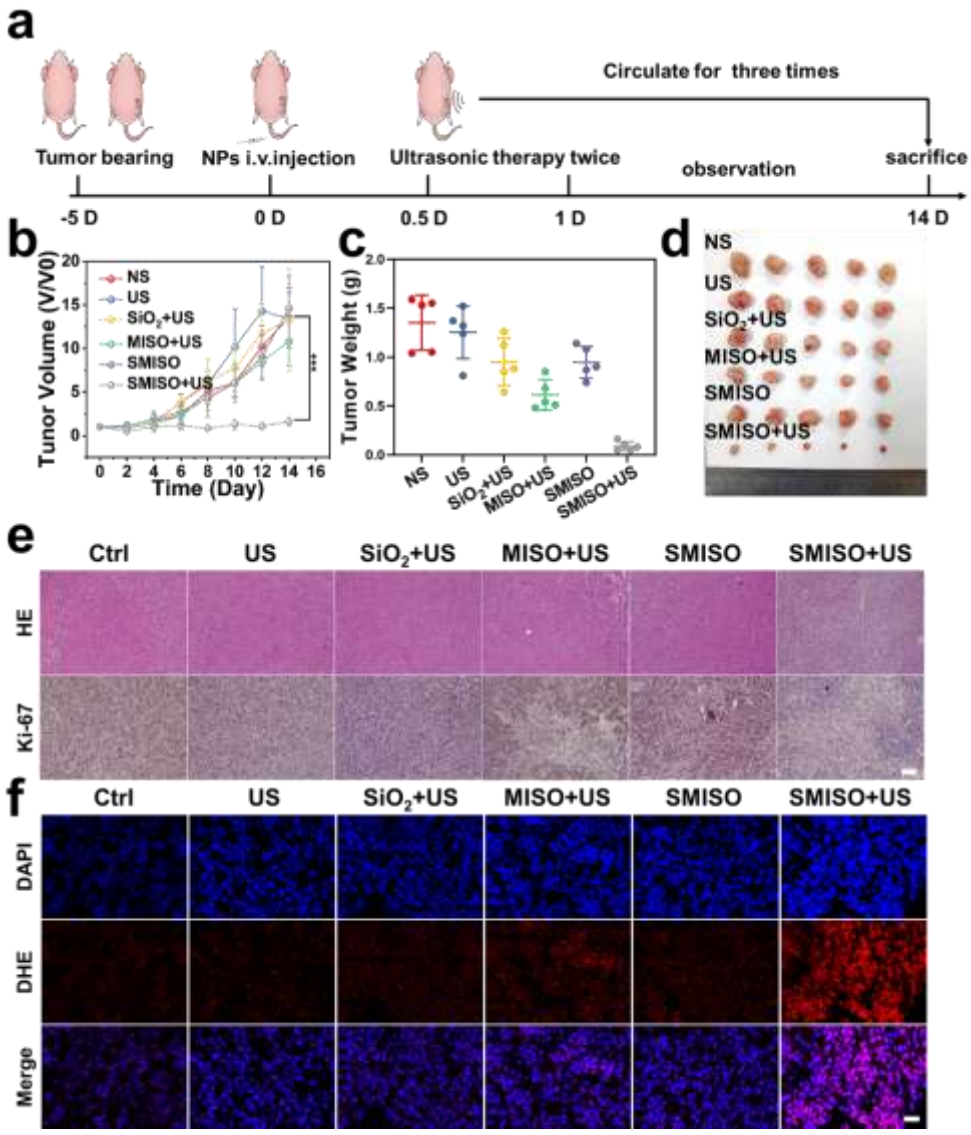

Figure 5. *In vivo* antitumor properties. (a) Schematic illustration of the *in vivo* SDT experiment on nude mice. The profiles of (b) tumor volume and (c) tumor weights of mice after different treatments (n = 5, mean ± SD). (d) Photographs of the tumors from the sacrificed mice of each groups on the 14th day. (e) H&E and Ki67 staining of the collected tumor slices after treatments (day-14). Scale bar: 100 μm. (f) Fluorescence images of tumor slices after DHE staining for ROS detection. Scale bar: 25 μm.*** $p < 0.001$.

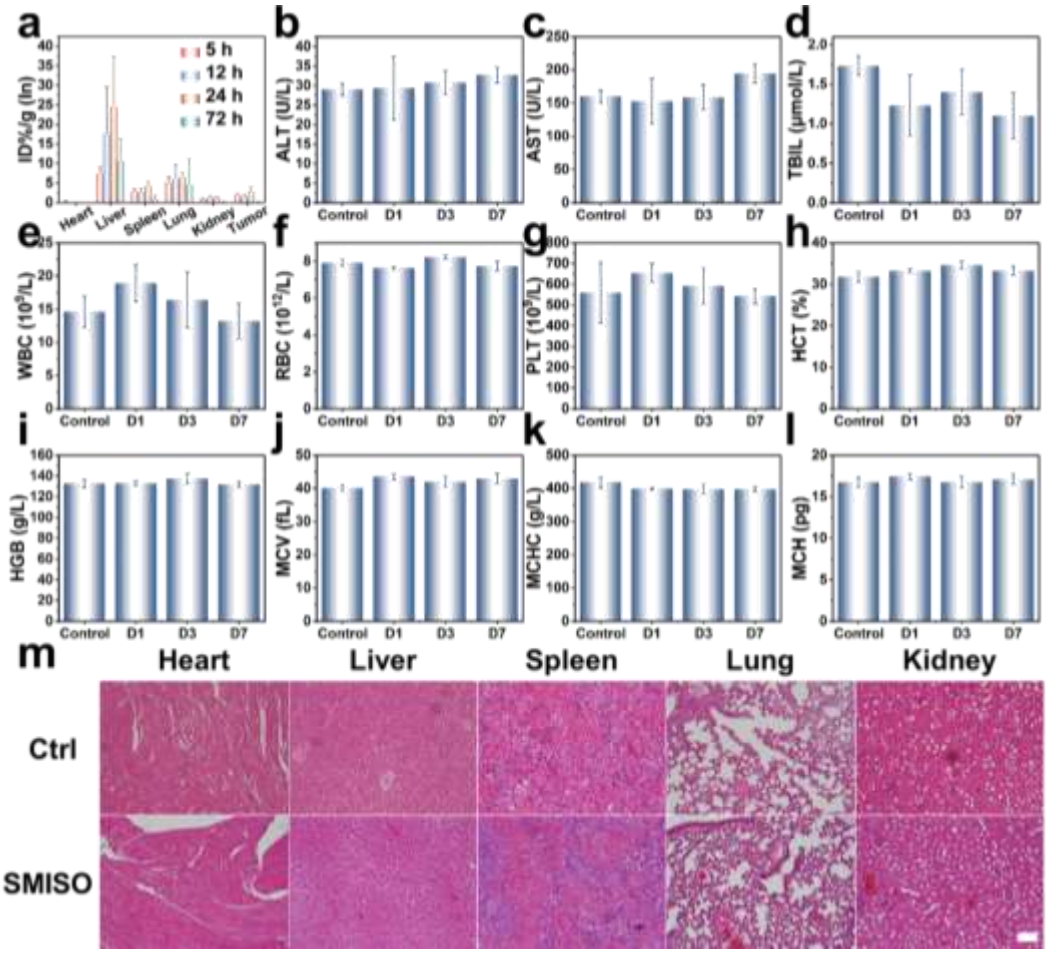

Figure 6. *In vivo* biosafety evaluation of SMISO NPs. (a) The biodistribution of In in the main organs (heart, liver, spleen, lung and kidney) of the mice after i.v. injection of SMISO for 5, 12, 24 and 72h. Blood biochemistry and hematological analysis of mice after i.v. injection of SMISO collected at 1st , 3rd and 7th days, including (b) alanine aminotransferase (ALT), (c) aspartate aminotransferase (AST), (d) total bilirubin (TBIL), (e) white blood cell (WBC), (f) red blood cell (RBC), (g) blood platelet (PLT), (h) hematocrit (HCT), (i) hemoglobin (HGB), (j) mean corpuscular volume (MCV), (k) mean corpuscular hemoglobin concentration (MCHC) and (l) mean corpuscular hemoglobin (MCH). (m) pathological examination of the changes in the main organs (heart, liver, spleen, lung and kidney) of the mice with or without i.v. injection of SMISO using H&E staining. Scale bar: 100 μm.

Table of Content